

<sup>1</sup> PREPARED FOR SUBMISSION TO JINST

<sup>2</sup> **Directional Xenon Measurement**

---

<sup>3</sup> ABSTRACT: Abstract...

<sup>4</sup> KEYWORDS: Only keywords from JINST's keywords list please

<sup>5</sup> ARXIV EPRINT: [1234.56789](https://arxiv.org/abs/1234.56789)

---

<sup>6</sup> **Contents**

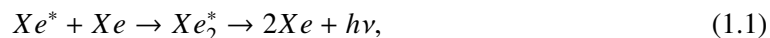
<sup>7</sup> <b>1</b>	<b>Introduction</b>	<sup>1</sup>
<sup>8</sup> <b>2</b>	<b>Experimental Setup</b>	<sup>2</sup>
<sup>9</sup>	2.1 The gas handling system	<sup>2</sup>
<sup>10</sup>	2.2 The cryogenic system	<sup>4</sup>
<sup>11</sup>	2.3 The detector system	<sup>5</sup>
<sup>12</sup>	2.4 The data acquisition system	<sup>7</sup>
<sup>13</sup> <b>3</b>	<b>Optical properties of the sphere</b>	<sup>9</sup>
<sup>14</sup> <b>4</b>	<b>Detector sensitivity</b>	<sup>9</sup>
<sup>15</sup> <b>5</b>	<b>Summary</b>	<sup>12</sup>

---

<sup>16</sup> **1 Introduction**

<sup>17</sup> The use of Noble-liquid detectors in the field of astroparticle physics has increased in the past  
<sup>18</sup> decades. Detectors aiming at measuring Dark Matter (DM) particles and neutrinos properties use  
<sup>19</sup> large liquid argon or liquid xenon (LXe) chambers [1, 2]. Current and future experiment for DM  
<sup>20</sup> detection are tuned to detect weakly interacting massive particles (WIMPs), a postulated candidate  
<sup>21</sup> for DM particle [3]. LXe based detectors are to date the leading in sensitivity and size for these  
<sup>22</sup> searches [4–7].

<sup>23</sup> When a particle interacts within the LXe media, it forms a cloud of excited and ionized states  
<sup>24</sup> with typical length of 100 nm. The excited Xe ( $Xe^*$ ) combines with other Xe atoms to form an  
<sup>25</sup> excited dimer state (excimer) when they decay to ground state they emit light.



<sup>26</sup> The electrons emitted from the ionization can recombine with a surrounding atom, this process of  
<sup>27</sup> recombination provides another possibility to produce excimers,



<sup>28</sup> Once  $Xe^*$  is produced it adds to the scintillation process explained in 1.1. There are two types of  
<sup>29</sup>  $Xe_2^*$  excimer states, singlet and triplet, with lifetime of  $\sim 3$  ns and  $\sim 25$  ns respectively. The wave-  
<sup>30</sup> length emitted by these states is between (175-180) nm which is lower than the lowest excitation of  
<sup>31</sup> xenon, and therefore travel through it to reach a photo-detector situated outside the LXe. Although

32 much is measured on these scintillation processes, the basic knowledge of the quantum properties  
33 of these interactions is based on experiments preformed several decades ago.

34 The phenomenon of superradiance in which identical quantum states "communicate" through  
35 electromagnetic field if in close proximity, is well studied. In certain conditions the emission of  
36 photons from these correlated states is very different then the sum of random states. This difference  
37 is in spectral, temporal and spatial properties [8, 9]. Early studies show that scintillation in LXe can  
38 produce coherent amplification of light [10, 11]. These studies were focusing on the macroscopic  
39 ionization using high energy density electron beams.

40 The understanding and quantification of the microscopic effects of non linear phenomena such  
41 as superradiance in Lxe for a single interaction, can improve DM experiments to reduce back-  
42 ground by the extra knowledge of directionality. irreducible background such as coherent neutrino  
43 nucleus scattering of neutrinos from the sun can be discard.

44 In this paper we present an experimental set-up called DIREXENO (Directional Xenon) aiming  
45 at measuring the spatial distribution of LXe scintillation light, and quantify non-isotropic emis-  
46 sion.

## 47 2 Experimental Setup

48 In order to identify superradiance effects in LXe, the temporal and spatial properties of scintillation  
49 events should be studied and quantified. In the DireXeno system LXe is circulated through a  
50 small spherical cavity held in a thick sphere made of high purified fused silica (HPFS). The sphere  
51 is surrounded ( $\sim 4\pi$ ) by PMTs allowing high resolution spatial and temporal measurements of  
52 individual photons. The PMTs do not come in contact with the xenon, so less impurities are  
53 introduced to it, and the material selection is less stringent. The geometrical design of the system  
54 approximates a point source of scintillation photons, and a detailed vertex reconstruction within  
55 the LXe bubble is unnecessary. A schematic view of the system is shown in Fig 1 .

56 The current system is designed with **TODO check digitization time**  $\sim 1$  ns time resolution, less  
57 than 1 ns synchronization between PMTs, and  $\sim 8$  radians spatial resolution. Since the exact nature  
58 and magnitude of superradiance in LXe is yet unknown a guiding principle in the design was flexi-  
59 bility to upgrades or redesign of any part of the system to fulfill any future experiment requirements.  
60 The modular design allows gain fast and easy recovery in case of components malfunction.

61 The system is made of four main building blocks. (i) **The gas handling system** which in  
62 normal working mode circulates the xenon and purifies it. (ii) **The cryogenic system**, liquefies the  
63 xenon and delivers it to the detector system. (iii) **The detector system** consists of a fused silica  
64 sphere that holds a small bubble of LXe target, and PMTs around the sphere. (iv) **The DAQ system**  
65 supplies high voltage (HV) to the PMTs and handles monitoring, triggering and digitization of data.  
66 The entire assembly is held on 3 separate racks as shown in Fig. 2 .

### 67 2.1 The gas handling system

68 In DIREXENO only the prompt scintillation is measured, so a high level of LXe purity is not of a  
69 great importance. However in many LXE detectors the desired level of impurity concentration is  
70 at the level of 1 ppb  $O_2$  equivalent [1] This is crucial to allow ionization electrons drift for several  
71 cm. To reach that purity level in a reasonable amount of time (several days instead of months), a

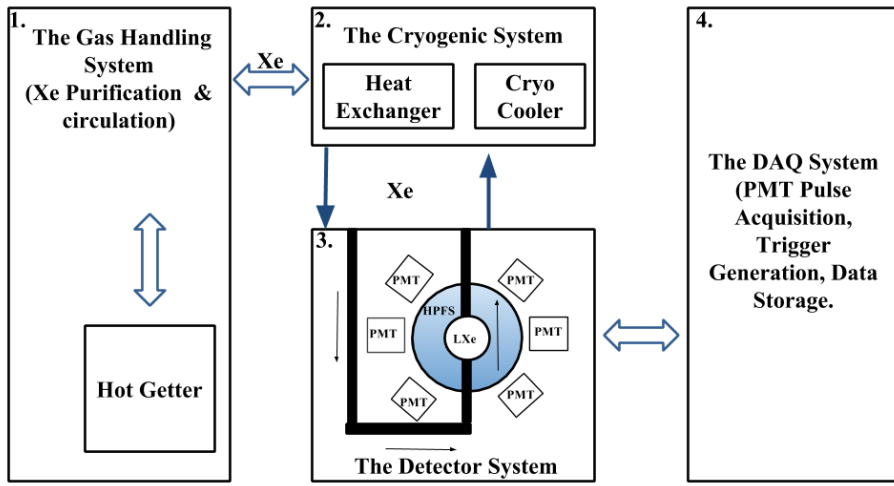


**Figure 1.** A schematic view of DIREXENO.

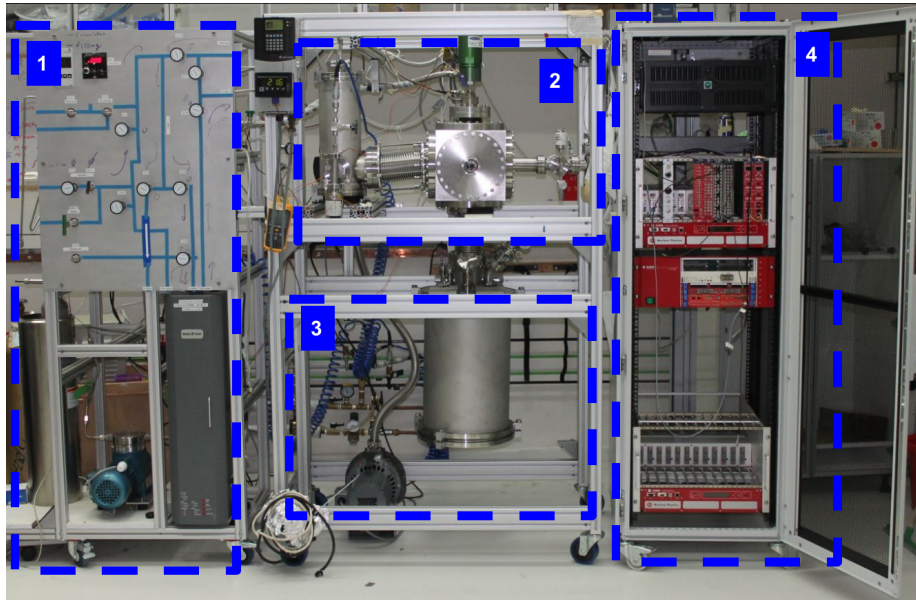


**Figure 2.** The DireXeno system mounted on the three racks. 1. The gas handling system. 2. The cryogenic system including the heat exchanger. 3. The detector chamber. 4. The Data acquisition system.

continuous purification is needed. The gas handling system provides this process along with all gas handling operations such as filling and recuperation and circulation. The xenon circulation also plays a major role in heat transfer.

During purification, The xenon is forced by a circulation pump<sup>1</sup> extracting LXe from the detector part through a heat exchanger<sup>2</sup> where it is heated and vaporized, into a hot getter<sup>3</sup> which cleans the xenon. The xenon passes through a mass flow controller<sup>4</sup> (MFC), enabling monitoring and controlling the amount of heat introduced to the system. Once purified, the xenon is delivered back to the cryogenic system via the heat exchanger, where the remaining GXe is liquefied before flowing back to the detector part. A schematic of this system is shown in fig. 3.

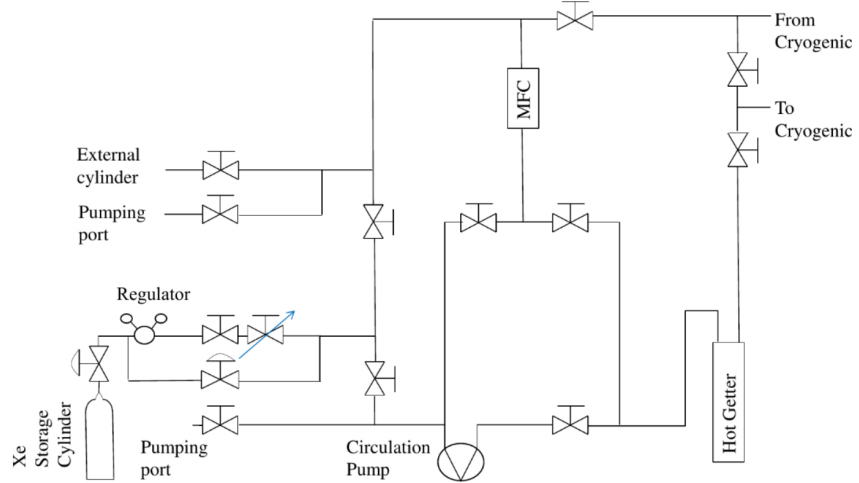


**Figure 3.** Schematics of the gas handling system. High pressure valves are indicated as valves with arcs. Needle valves are indicated as a valve with an arrow.

## 2.2 The cryogenic system

Remote cooling is generally used in LXe experiments due to reduction in background radiation and acoustic noise from the cooler to the detector, and due to design flexibility. The cryogenic system is connected to the gas handling system on one side and to the detector part on the other, and built such that replacing the cryo-cooler type (e.g., to PTR) requires just an adaptation to the top flange.

The cryogenic system is divided to an outer vessel (OV) which holds the insulation vacuum, and an inner vessel (IV) which holds the xenon. In addition to the vacuum which prevents heat leakage due to diffusion and convection, the IV is completely covered by multi layer aluminized Myler to prevent heating via radiation.

The OV is made of a 10" Conflat (CF) cube, with ports on all six faces, interfacing the gas handling system and the detector part, and bearing service ports (e.g., feed-throughs, pumping ports, view ports). The OV is connected to the detector part via a 6" CF flexible bellows, providing a shared vacuum.

The IV is made of 1.5" long cylinder with 6" CF flanges on both sides, holding xenon within. A 120 mm diameter cold finger is welded to its top flange. The design of the cold finger is similar to the one in [12]. The inner part of the cold finger is made of long fins, resulting in a better heat

<sup>1</sup>N143 SN.12E AC 230V50HZ KNF diaphragm circulation pump

<sup>2</sup>GEA GBS100M-24 plate heat exchanger

<sup>3</sup>MONO-TORR PS4-MT15-R-2

<sup>4</sup>MKS mass flow controller 1179A00614CR1BM

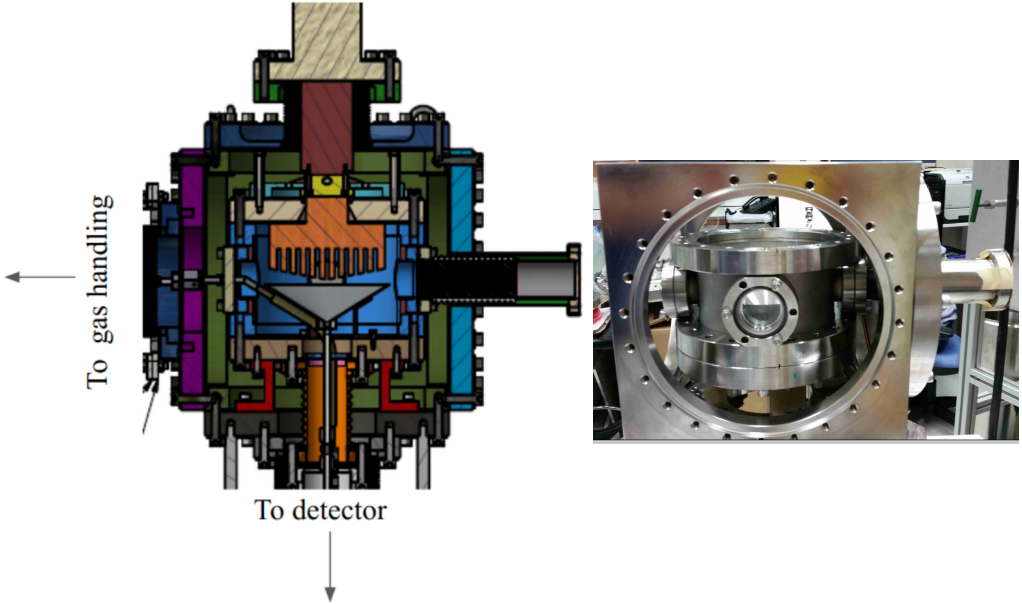


**Figure 4.** CAD view of the cryogenic system(Left) and a picture of the cryogenic system (Right) . The cryogenic system. (Left) CAD design view, (right) picture of the actual system.

97 transport. The upper part of the cold finger is in thermal contact with the QDrive cryo-cooler <sup>1</sup> via  
 98 a copper adapter. The copper adapter holds two  $100\Omega$  pt resistor which are connected to a PID  
 99 reader<sup>2</sup> for temperature measurements. A cartridge-heater is also inserted to the copper adapter for  
 100 emergency heating in case xenon freezes on the cold finger.

101 The cryo-cooler is connected via a  $4\frac{1}{2}$ " flange to the OV top flange. While usually cryo-coolers  
 102 used for xenon experiments constantly operate in maximal cooling, the QDrive cryo-cooler utilizes  
 103 a temperature control to vary its cooling power up to 70 W. This allows setting a desired working  
 104 temperature which is constant within less than  $0.1\text{ }^{\circ}\text{C}$  measured on the cryo-cooler.

105 On the inner side of the IV bottom flange a thin 0.6 mm SS funnel is installed collecting  
 106 LXe drops from the cold finger, and delivering them to the detector. This flange is attached to the  
 107 detector part, via a  $3\frac{3}{8}$ " flexible bellows. The bellows hosts two pipes connected to the circulation  
 108 system, and a third pipe coming from the funnel. The three pipes deliver LXe whereas the GXe is  
 109 filling the bellows volume. The purer LXe (from the gas handling system) and the less pure LXe  
 110 (from the cold finger) are separated, and can be delivered to different parts of the system. Some  
 111 of the guidelines for the design of the cryogenic system are based on [13]. The CAD view of the  
 112 design of the cryogenic system and a photo of the actual system are shown in Fig 4.

### 113 2.3 The detector system

114 The detector system refers to a vacuum chamber and its inner assembly consisting of a transparent  
 115 sphere that contains the LXe, the PMT sensors observing it and their accessories. This chamber is  
 116 placed below the cryogenic system.

<sup>1</sup>QDrive 20BB 9p6 A 3 AYNBNCO

<sup>2</sup>cryo-con model 18i Cryogenic Temp Monitor

117 The interface unit to the cryogenic system is built out of two flanges welded together via seven  
 118 tubes, which serve as service ports for electrical and other feedthroughs: four with a  $2\frac{3}{4}$  CF flange,  
 119 and three with a  $1\frac{1}{3}$  CF flange (mini-CF). The upper flange, ISO-K NW320, shares the cryogenic  
 120 system's OV insulation vacuum, while the bottom one, CF-10", is part of the IV and could hold  
 121 xenon for future detectors. The CF flange is also adapted to fit a smaller CF-4 $\frac{5}{8}$ " flange which is  
 122 currently used.

123 The vacuum chamber is made of an ISO-K NW320 nipple closed with a blank flange from  
 124 below, the length of the nipple is determined such that the maximal height of the whole apparatus  
 125 is 190 cm, allowing an easy transport of the detector through standard doors.

126 The 4 $\frac{5}{8}$ " CF flange is connected to a split vessel that serves as a LXe reservoir. one part is  
 127 connected to the top of the HPFS sphere, and one to the bottom. LXe is circulated such that LXe  
 128 coming from the gas system drips into one part and pumped from the other. This controls the liquid  
 129 level, and the sphere is constantly filled with LXe.

130 The sphere is a custom designed hollow shell made of Corning HPFS 8655 with high trans-  
 131mittance to VUV. Two Invar tubes with SS mini-CF flange are connected to the sphere on both  
 132 sides. The technical design and photo of the sphere are shown in Fig. 5. The optical properties  
 133 of the sphere will be further discussed in Sec. 3. The bottom flange of the sphere is held using a  
 134 brass holder to prevent force or torque applied on the sphere while mounting it. The brass holder  
 135 is connected to a plate held from the top CF-10" flange.

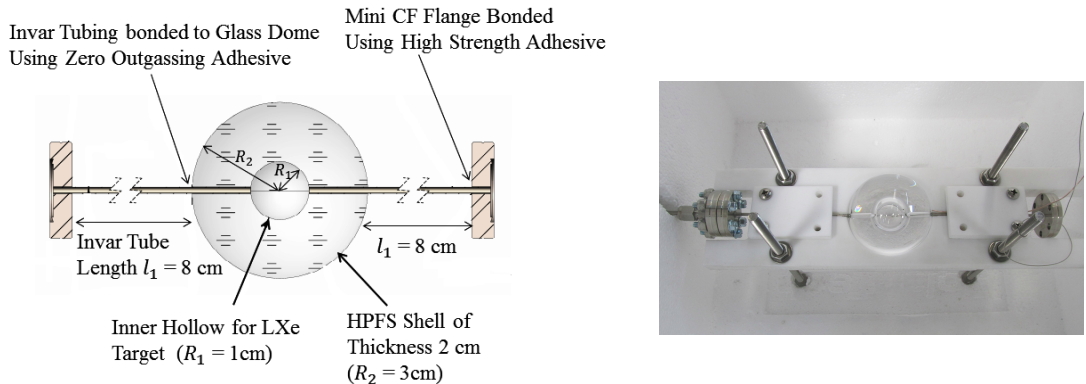


**Figure 5.** (Left)The technical design of the HPFS shell with Invar tubing and mini CF flanges. (Right) The industrially manufactured HPFS shell, held in a test fixture.

136 Photons emitted from the LXe in the sphere are detected by 20 PMTs<sup>1</sup>. The PMTs are chosen  
 137 to have a quantum efficiency greater than 30% at 178 nm. The gain of the PMTs is  $2 \times 10^6$  at  
 138 an applied voltage of 900 V . A positive voltage divider<sup>2</sup>, is used to provide high voltage to the  
 139 PMTs. The PMTs are held with a special aluminum holder, coated with anti-reflection substance.  
 140 The holder is made of two hemispheres hosting the PMTs in 3 rows all of them pointing to the  
 141 center of the sphere. The PMTs are attached to the holder by their voltage-divider bases using M2  
 142 PEEK screws (see Fig 6). The CAD design and a photo of the detector system are shown in Fig. 7.

<sup>1</sup>R8520-406 Hamamatsu 1" PMT, active area 20.5 mm  $\times$  20.5mm

<sup>2</sup>Hamamatsu VDS18130p 24 channel positve polarity.

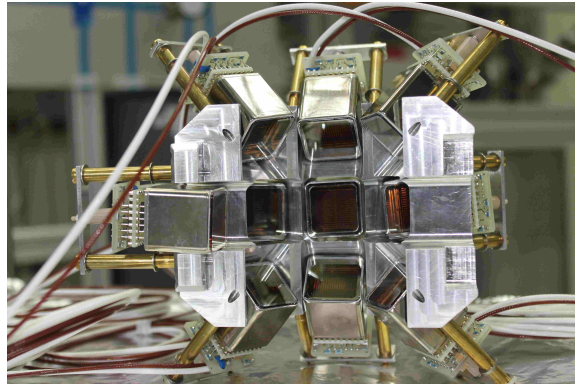


**Figure 6.** A PMT holder–hemisphere. Two identical hemispheres are used to hold the PMTS around the sphere.

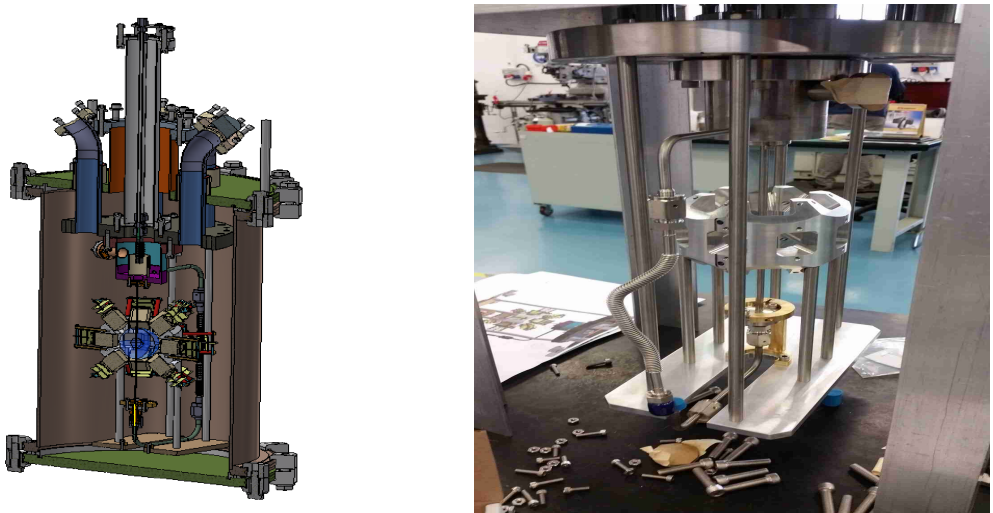


**Figure 7.** (Left) CAD design of the detector part. (Right) First mounting of the detector part, still not connected to the rest of the system.

#### 143 2.4 The data acquisition system

144 The DAQ system is heterogeneous using both NIM and VME electronic modules. The data readout  
 145 is being carried out through a PCIe card<sup>1</sup> connected via an optical link to a VME controller<sup>2</sup>. A  
 146 schematic layout of the DAQ system is shown in Fig. 8.

147 The PMTs are ramped up to +800V (the maximum is +900V) using VME high voltage dis-  
 148 tributor module<sup>3</sup>. The raw pulses from the PMTs are amplified and shaped using two PMT pream-  
 149 plifiers<sup>4</sup>. The preamplifier operates from DC to 275 MHz and produces two identical 50 Ω non  
 150 inverting outputs with voltage gains of 10 for each PMT channel. One of the outputs is converted

---

<sup>1</sup>CAEN A3818 PCIe

<sup>2</sup>CAEN V2718 VME controller

<sup>3</sup>iseg VDS18130p : 24 independent channels positive polarity voltage distributor

<sup>4</sup>Phillips 776. 16 independent and direct-coupled amplifiers channels

151 into a digital signal by an ADC<sup>1</sup>, and the other to binary signals using two discriminators <sup>2</sup>.

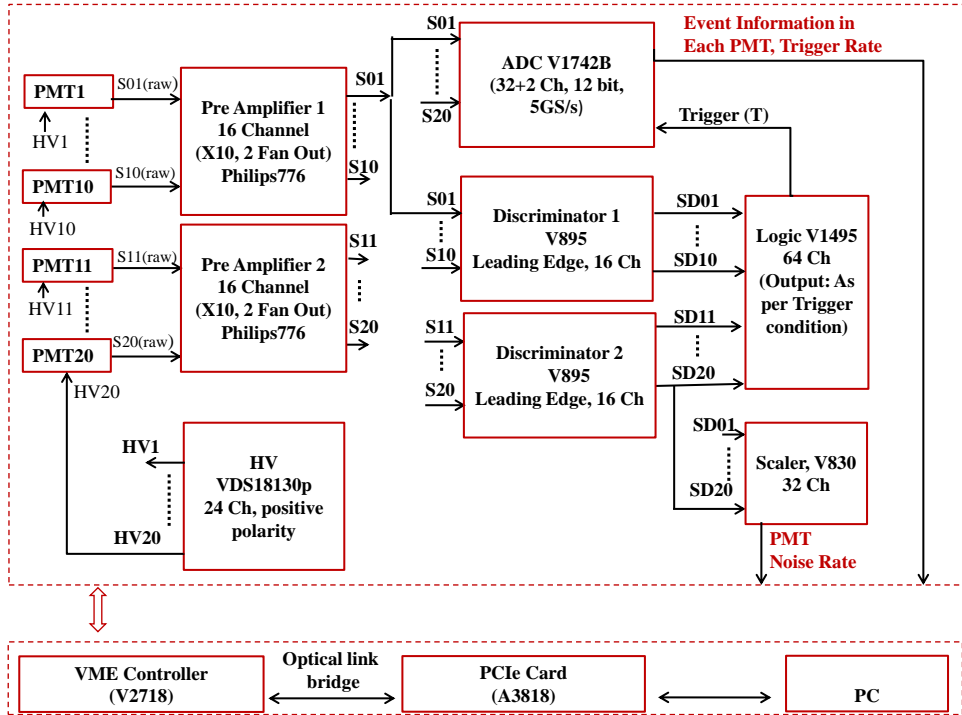


**Figure 8.** The schematic of the data acquisition system of DireXeno. The signal coming from 20 PMTs ( $i = 1 - 20$ ) and the subsequent electronic channels to record the events once triggered. Where  $S_i(\text{raw})$  is the raw electrical pulse output of the PMTs,  $S_i$  are the amplified pulses, and  $SD_i$  are the binary outputs from the discriminator.

152 The ADC consists of two 12bit 5GS/s switched capacitor digitizer sections, each of them with  
 153 16+1 channels, based on DRS4 chip. The dynamic range of the input signal is 1 Vpp with an  
 154 adjustable DC offset. This module constantly samples (5GS/s, 2.5 GS/s or 2 GS/s) either bipolar  
 155 or unipolar analog input signals, and records them into circular analog memory buffers. Once  
 156 triggered, all analog memory buffers are frozen and digitized into a digital memory buffer with a  
 157 12 bit resolution.

158 The binary output signals from the discriminator are duplicated and fed to the logic module<sup>3</sup>  
 159 and to a scaler<sup>4</sup>. A global majority trigger is generated in the logic module with the coincidence  
 160 of any two out of the twenty PMTs within a time window of **XXX ns**. The event information and  
 161 trigger rate are read from the ADC, while the individual PMTs trigger rate from the scaler. Further  
 162 analyses of the relevant events are carried out offline.

<sup>1</sup>CAEN ADC V1742: switched capacitor digitizer

<sup>2</sup>CAEN V895 16 channel leading edge discriminator

<sup>3</sup>CAEN V1495: FPGA based general purpose VME board

<sup>4</sup>CAEN V830: 16 channel scalar

### 163 3 Optical properties of the sphere

164 The central component of the experiment is the HPFS sphere, which holds the LXe target, located  
 165 in the center of the detector system. The sphere is made of two Corning HPFS 8655 hemispheres  
 166 attached by a UV transparent glue. The refractive index of this HPFS is 1.58 at 185 nm, matching  
 167 to the LXe one, which is 1.61. Hence, there is minimal diffraction from the original direction of  
 168 the photons as they transit from the LXe target to the sphere. The refractive index at various  
 169 wavelengths are shown in Fig. 9 (left panel).

170 The HPFS transparency to VUV photons is an extremely crucial parameter for setting the  
 171 sphere's dimensions (inner and outer radii) and detector sensitivity. Therefore, the transmittance  
 172 of an HPFS sample was measured, using a VUV monochromator light source. The measured  
 173 transmittances as a function of wavelength are shown in Fig. 9 (right panel). The transmittance of  
 174 the sample at 178 nm, is  $\sim 98.7\%/\text{cm}$ .

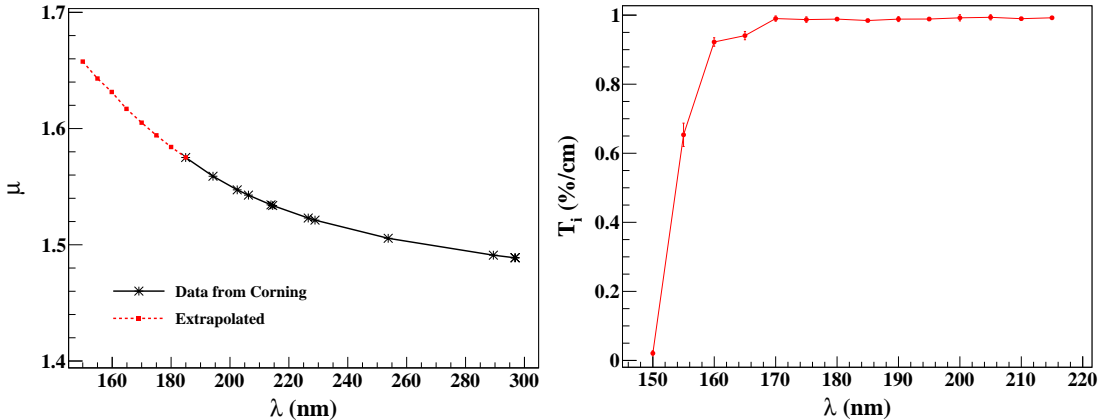


Figure 9. Some relevant characteristics of HPFS-8655. (Left) The refractive index as provided by corning and extrapolated to relevant wavelength range. (Right) The internal transmittance ( $T_i$ ). Say something about the error bars

175 The sources that will be used for exciting the xenon, and creating the superradiance (signal)  
 176 as well as the standard emission (background), will be  $^{137}\text{Cs}$  ( $E_\gamma=662\text{ keV}$ ) and  $^{57}\text{Co}$  ( $E_\gamma=122\text{ keV}$   
 177 &  $136\text{ keV}$ ) for ER with mean free path of  $\sim 4\text{ cm}$  and  $\sim 1\text{ cm}$  respectively. For NR  $^{241}\text{AmBe}$ ,  
 178 D-D neutron generator, or neutron produced in an accelerator will be used.

179 Using a GEANT4 based simulation [14] studying the path of the scintillation photons the  
 180 sphere dimensions are optimized. The shell should be thick enough to reduce internal reflections,  
 181 but not too thick to attenuate the scintillation light. The LXe target bubble within should not be too  
 182 large in order to avoid double scatters. The outer radius is 3 cm, and the inner (the hollow space  
 183 that holds the LXe) is 1 cm.

### 184 4 Detector sensitivity

185 The sensitivity of the detector is estimated by its ability to identify an anisotropic component in the  
 186 scintillation photons emission pattern (signal), over the isotropic one (background). The photon

187 emission pattern is modeled using a combination of isotropic emission and one or two beams:

$$\mathcal{F}(\theta, \phi) = (1 - r_{aniso}) \cdot f_{iso} + r_{aniso} \cdot [r_1 f_G(\sigma_1) + r_2 f_G(\sigma_2)], \quad (4.1)$$

188 where  $f_{iso}$  is the PDF of an isotropic emission,  $f_G$  is a PDF of a Gaussian distribution with half  
 189 width  $\sigma$ .  $r_{aniso}$  is the anisotropic emission fraction, and  $r_{1,2}$  are the relative beams intensities. The  
 190 first beam direction is random, and the second's is either random ("uncorrelated") or opposite to  
 191 the first's ("correlated"). The different emission patterns used here are summarized in Table 1.

**Table 1.** Anisotropic emission patterns. For all patterns  $r_{aniso} = 0.1$

Pattern no.	No. of beams	type	Beam half widths		Signal fractions		$N'$
			$\sigma_1$	$\sigma_2$	$r_1$	$r_2$	
1	1	single beam	5°	-	1	0	3200
2	1	single beam	15°	-	1	0	4630
3	2	correlated	5°	5°	0.5	0.5	4520
4	2	correlated	15°	15°	0.5	0.5	9770
5	2	uncorrelated	5°	5°	0.5	0.5	9370
6	2	uncorrelated	5°	10°	0.5	0.5	19500
7	2	uncorrelated	15°	15°	0.5	0.5	28200
8	2	uncorrelated	10°	30°	0.5	0.5	49900
9	2	uncorrelated	10°	30°	0.2	0.8	56000
10	2	uncorrelated	30°	10°	0.2	0.8	43000

192 A GEANT4 based simulation is used to model the detector system, generate photons, propagate  
 193 them through the detector, and obtain a PMT hit pattern. The photons detected at the PMTs  
 194 are mapped and put through a statistical test to check the detector's sensitivity towards the different  
 195 emission patterns.

196 The relevant geometrical and optical parameters, which are used in the simulation, are listed  
 197 in Table 2. The scintillation light produced in a particular event is emitted by a cloud of excimers.  
 198 This cloud is assumed to have a linear size much smaller than that of the optical system. Therefore  
 199 each event is simulated as a number of photons that are emitted from a point in the LXe with some  
 200 emission pattern (see Table 1). The number of generated photons for each event is taken to be  
 201 Poisson(50), which correspond to an energy deposition of  $\sim 2.5\text{keV}$  or  $\sim 7\text{keV}$  for ER or NR  
 202 respectively. The LXe target is much smaller than the mean free path of the source particles, and to  
 203 account for that the events are uniformly generated in the LXe volume. The probability for a photon  
 204 being transmitted/reflected at a given surface is determined by Fresnel's equations, which include  
 205 Snell's law for the transmitted light, and specular reflection for the reflected light. The boundary  
 206 surfaces between different media such as, the LXe–HPFS, HPFS–vacuum and vacuum–PMT, are  
 207 assumed to be perfectly smooth, therefore enabling only specular reflection. The photons reaching  
 208 the PMTs can either be detected, absorbed or reflected from the photocathode or PMT window. A  
 209 simplified approach of the above possibilities is considered: a photon reaching the PMT has a 30%  
 210 probability to be detected (since the PMTs have  $\text{QE} \geq 30\%$ ), 50% probability to get absorbed and  
 211 20% probability to get specularly reflected.

**Table 2.** The parameters used in simulation

Parameter	Value	Parameter	Value
LXe absorption length	100 cm	HPFS shell inner radius	1cm
LXe scattering length	35 cm	HPFS shell thickness	2 cm
LXe refractive index	1.61	PMT QE	30%
LXe Scintillation wavelength	178	PMT distance from center	39 mm
HPFS absorption length	100 cm	Number of PMT	20
HPFS refractive index	1.57	PMT active area	22mm × 22mm
HPFS scattering length	$\infty$	Invar tube diameter	1 mm

212      The statistical fluctuation in the electronic signal generated in a PMT for a certain number of  
 213      incident photon is taken into account. The R8520 PMTs have 20% probability for double photo-  
 214      electric emission for 178 nm photons, which is included in the simulation. Each detected photon  
 215      on a PMT is assigned a uniformly random position on the PMT surface. The direction of this  
 216      point with respect to the center of the LXe sphere is defined as the incident direction of the photon.  
 217      The direction information is then used to calculate the angles between all possible pairs of pho-  
 218      ton for any event and calculate the correlation between all angle pairs. **Do you want to add fig of**  
 219      **correlations iso and aniso?**

220      In order to quantify the anisotropy of the emission, the angle correlation distribution of an  
 221      anisotropic hit pattern is compared to that of the isotropic pattern. A  $\chi^2$  test statistics is used where  
 222      the reduced  $\chi^2$  is defined as:

$$\chi^2_\nu = \frac{1}{\nu} \sum_{i=1}^{\nu} \frac{(O_i - E_i)^2}{E_i}, \quad (4.2)$$

223      where  $E_i$  is the expected number of entries for an isotropic emission obtained from a sample  
 224      of  $10^5$  simulated events.  $O_i$  is the observed number of entries, and  $\nu$  is the total number of angle  
 225      correlation bins which is also the degree of freedom. Sixty bins of identical width are used.

226      To asses the needed exposure to claim discovery assuming one of the pattern mentioned above,  
 227       $10^4$  data sets are generated and tested against the null hypothesis. This is repeated for increasing  
 228      number of events between 1 – 4000 assuming different values of the anisotropy fraction ( $r_{aniso}$ ).  
 229      The  $\langle \chi^2_\nu \rangle$  and its  $2\sigma$  band for pattern 1, assuming  $r_{aniso} = 0.1$  overlaid with the corresponding  
 230      values for an isotropic emission are shown in Fig. 10. The values of  $N'$ , required to claim  $5\sigma$   
 231      discovery, for different values of  $r_{aniso}$  are calculated for each pattern as illustrated in Fig. 11. The  
 232      number of events  $N'$  for  $r_{aniso} = 0.1$  are summarized in Table 1 for all emission patterns.

233      A simulation with two typical sources that emit isotropically, a  $10 \mu\text{Ci}^{137}\text{Cs}$  (662 keV gamma),  
 234      and a  $2.7 \mu\text{Ci}$  AmBe (5 MeV neutron), shows that for an average yield of 50photons/event, the rate  
 235      of events in the detector is:  $1.25 \times 10^4$  events/day for NR and 625 events/day for ER. Therefore a  
 236      system that can operate stably for few weeks is expected to do reasonable measurements for ER  
 237      and NR events.

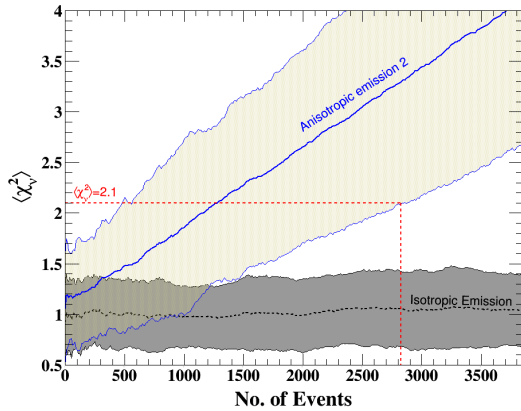


**Figure 10.**  $\langle \chi^2 \rangle$  and its  $2\sigma$  band for isotropic emission (black) and for pattern 2 (blue). The  $\langle \chi^2 \rangle$  for isotropic emission fluctuate around 1 with  $\sigma = 0.2$  which is consistent with the expected value of  $\frac{1}{\sqrt{30}} \equiv 0.18$  for reduced  $\chi^2$  distribution with 60 degrees of freedom.  $\sim 3000$  events are needed to claim  $5\sigma$  discovery ( $\chi^2 = 2.1$ ) for this emission pattern

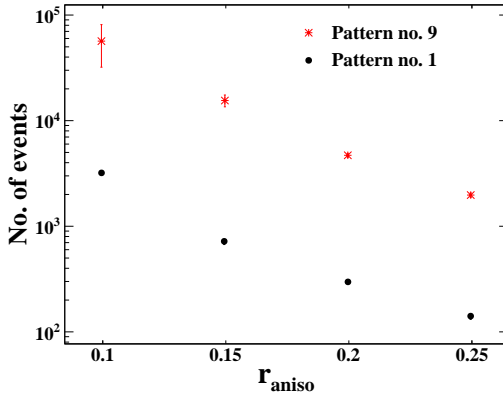


**Figure 11.** The number of events needed for each emission pattern to achieve  $5\sigma$  presented only for pattern 1 and 9. Here  $r_{aniso} = 0.1$ . for four different values of  $r_{aniso}$ .

## 238    5 Summary

239    The setup of Direxeno, an experiment to measure the spatial and temporal distribution of LXe  
 240    scintillation, has been presented. The system consists of 4 main building blocks (gas handling,  
 241    cryogenic, detector, and DAQ), each of which can be exchanged without altering others allowing  
 242    significant flexibility and modularity. Each of the building blocks has been described in detail, with  
 243    emphasis on the design and components.

244    The sensitivity of the setup to different postulated non isotropic emission patterns are studied  
 245    using MC simulations. For the patterns studied, a run-time of 2-3 weeks is required using typical  
 246    radioactive sources. Therefore the system is designed to maintain stability over a reasonable time  
 247    period.

248    Using DireXeno, effects like superradiance or any other non-linear scintillation can be mea-  
 249    sured. Measuring the correlation between the direction of the emission and the direction of the

250 radioactive source, may lead to directionality measurement which will allow enhanced statistical  
251 modeling of background and improved sensitivity in DM experiments.

## 252 References

- 253 [1] E. Aprile and T. Doke. Liquid Xenon Detectors for Particle Physics and Astrophysics. *Rev. Mod.*  
254 *Phys.*, 82:2053–2097, 2010.
- 255 [2] A. Rubbia. Future liquid Argon detectors. 2013. [*Nucl. Phys. Proc. Suppl.* 235-236, 190(2013)].
- 256 [3] J. Silk et al. *Particle Dark Matter: Observations, Models and Searches*. Cambridge Univ. Press,  
257 Cambridge, 2010.
- 258 [4] E. Aprile et al. First Dark Matter Search Results from the XENON1T Experiment. 2017.
- 259 [5] D. S. Akerib et al. Results from a search for dark matter in the complete LUX exposure. *Phys. Rev.*  
260 *Lett.*, 118(2):021303, 2017.
- 261 [6] Changbo Fu et al. Spin-Dependent Weakly-Interacting-Massive-Particle–Nucleon Cross Section  
262 Limits from First Data of PandaX-II Experiment. *Phys. Rev. Lett.*, 118(7):071301, 2017.
- 263 [7] J. Aalbers et al. DARWIN: towards the ultimate dark matter detector. *JCAP*, 1611:017, 2016.
- 264 [8] R. H. Dicke. Coherence in spontaneous radiation processes. *Phys. Rev.*, 93:99–110, Jan 1954.
- 265 [9] M. Gross and S. Haroche. Superradiance: An essay on the theory of collective spontaneous emission.  
266 *Physics Reports*, 93(5):301 – 396, 1982.
- 267 [10] N G Basov, V A Danilychev, and Yurii M Popov. Stimulated emission in the vacuum ultraviolet  
268 region. *Soviet Journal of Quantum Electronics*, 1(1):18, 1971.
- 269 [11] Frederick H. Mies. Stimulated emission and population inversion in diatomic bound-continuum  
270 transitions. *Molecular Physics*, 26(5):1233–1246, 1973.
- 271 [12] E. Aprile et al. The XENON100 Dark Matter Experiment. *Astropart. Phys.*, 35:573–590, 2012.
- 272 [13] K L Giboni, X Ji, H Lin, A Tan, T Ye, Y Zhang, and L Zhao. A liquid xenon development and test  
273 system. *Journal of Instrumentation*, 9(04):T04006, 2014.
- 274 [14] S. Agostinelli et al. Geant4 a simulation toolkit. *Nuclear Instruments and Methods in Physics*  
275 *Research Section A: Accelerators, Spectrometers, Detectors and Associated Equipment*, 506(3):250 –  
276 303, 2003.